Variations in sea surface temperature due to near surface straining flow

Andrew Wells

October 1, 2007

Abstract

The dynamics of the thermal boundary layer below the free surface of the ocean can be influenced by flows generated in the fluid interior, resulting in changes in sea surface temperature. These thermal boundary layer dynamics are studied using laboratory experiments with upwelling flows. The measured surface temperature is well described by a non-dimensional formulation of previous theoretical results. This non-dimensional formulation allows us to predict that internal waves are unlikely to be responsible for large changes in sea surface temperature, but could have an important effect on the transfer of gases between the ocean and atmosphere.

1 Introduction

Detailed modelling of the atmosphere and ocean requires knowledge of the sea surface temperature, which influences the exchange of heat and mass across the air–water interface. Small changes in sea surface temperature can significantly effect the air–sea heat exchange and also change evaporation rates at the interface, leading to modifications in near surface salinity. As a result, the thermal boundary layer near to the ocean surface, or *skin layer*, has recently been an area of active research interest (e.g. Castro *et al.*, 2003; Soloviev, 2007). The thermal boundary layer plays an important role in controlling the sea surface temperature, yet it lies at too small a scale to be resolved in global climate models or field observations. The influence of the thermal boundary layer on sea surface temperature must therefore be parameterised, and so a detailed understanding of the boundary layer dynamics is required in order to provide an accurate parameterisation of the unresolved physics (Fairall *et al.*, 1996). We present a discussion of the effects of upwelling and downwelling flow on sea surface temperature and experimentally investigate the resulting dynamics of the thermal boundary layer.

Some of the pioneering measurements of the ocean skin layer were conducted by Woodcock & Stommel (1947), who observed colder temperatures close to the surface than in the interior of salt and fresh water ponds. This has been followed by numerous field, laboratory, theoretical and numerical studies. For low wind speeds a free convective boundary layer develops, as summarised by Katsaros (1980). The dynamics are modified slightly in the presence of strong winds (see Saunders, 1967; Castro *et al.*, 2003, for example), with additional shear generated turbulence acting to thin the thermal boundary layer. The near-surface boundary layer may also be modified by the presence of surface waves (see Katsaros, 1980,

for a review), or surfactants (McKenna & McGillis, 2004). The dynamically similar problem of air-sea gas transfer has also received considerable attention (Soloviev & Schlüssel, 1994; Soloviev *et al.*, 2007).

There have been comparatively fewer studies of the effect of sub-surface flows on the free surface temperature. Infrared observations of the sea surface temperature have shown banded thermal signatures consistent with the scales of internal waves (Walsh *et al.*, 1998; Marmorino *et al.*, 2004; Zappa & Jessup, 2005; Farrar *et al.*, 2007). This suggests that flow structures generated within the ocean interior may be responsible for modifying the properties of the near surface thermal boundary layer. An increase in surface temperature had also qualitatively been observed above an upwelling jet flow in the experiments of Ewing & McAlister (1960). Osborne (1965) presented a theory to describe the modulation of surface temperature by waves and other flows, and Leighton *et al.* (2003) used direct numerical simulation to consider the effect of the local straining flow generated by convection cells. However, there has been no detailed investigation of the dynamics described by the Osborne (1965) theory.

We present a quantitative experimental investigation of the dynamics of the thermal boundary layer in the presence of a local upwelling flow. In §2 we review the details of previous theoretical treatments of the free convective boundary layer and the modifications resulting from a straining flow applied near to the surface. A non-dimensional formulation is presented that identifies different dynamical regimes for the thermal boundary layer, with a corresponding difference in the resulting sea surface temperature. The non-dimensional formulation allows us to identify the relevant regime for flows in the laboratory, and also in the ocean. The experimental procedure and results are described in §3 and §4, respectively. We observe a local increase in surface temperature above regions of upwelling flow, and show that the Osborne (1965) and Leighton *et al.* (2003) theories both provide an accurate description of the observed difference between the free surface and bulk temperatures. We conclude with a discussion of implications for climate modelling in §5. A simple application of the Osborne (1965) theory suggests that internal waves produce only a small effect on sea surface temperature via the skin layer straining mechanism, but could be responsible for significant change in ocean-atmosphere gas transfer.

2 Theoretical Background

The cool skin of the ocean can be considered as a laminar thermal boundary layer occurring where oceanic turbulence is suppressed close to the free surface. The surface of the ocean is cooled by radiative, evaporative and sensible heat fluxes from the ocean to the atmosphere. The transfer of heat is purely by molecular conduction just below the ocean surface. Conservation of enthalpy across the air–water interface requires that the sub-surface conducted heat flux must balance Q, the loss of heat to the atmosphere, so that

$$-\rho c_p \kappa \left.\frac{\partial T}{\partial z}\right|_{z=0} = Q = Q_{\mathrm{rad}} + Q_{\mathrm{evap}} + Q_{\mathrm{sens}}. \tag{1}$$

The radiative component of ocean to atmosphere heat flux is denoted by Q_{rad}, with Q_{evap} and Q_{sens} the corresponding evaporative and sensible heat flux components, respectively. Typically $Q \approx 200\,\mathrm{W\,m^{-2}}$ for a daytime ocean to atmosphere heat flux (see Wick *et al.*,

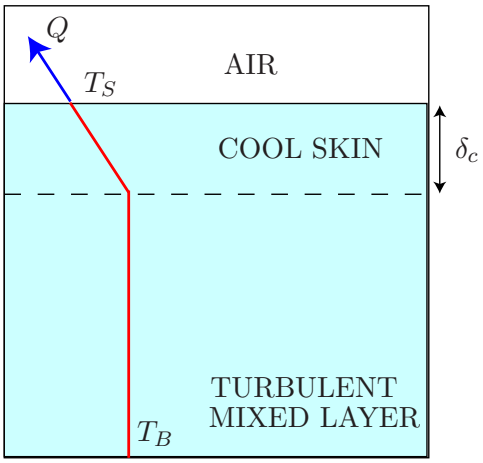

Figure 1: Schematic model of the surface thermal boundary layer of the ocean. A cold, laminar conductive boundary layer overlies a turbulent well mixed interior.

1996, for example.).[1] The ocean is confined to $z < 0$ and has temperature T, with density ρ, specific heat capacity c_p and thermal diffusivity κ. The removal of heat at the upper surface leads to the formation of a thermal conductive boundary layer just below the surface of the ocean. As we move deeper into the fluid the laminar surface layer breaks down due to turbulent velocity and temperature fluctuations and we have a fully turbulent mixed layer, as shown schematically in figure 1. Oceanic turbulence can be generated by buoyant convection or by a surface wind stress, and acts to maintain a relatively uniform temperature down to depths of metres or more.

2.1 Convective boundary layer in absence of imposed flow

For relatively calm conditions with negligible imposed wind shear, the dominant source of mixed layer turbulence is from the buoyancy supplied by cooling at the ocean surface. The dynamics of the resulting convective flow is well described by surface renewal models (Soloviev & Schlüssel, 1994) which build on the analysis of Howard (1966) for convection below a cooled surface. The ocean surface acts as an effectively impermeable upper boundary, so that turbulence is suppressed in a laminar layer immediately below the surface. The removal of heat into the atmosphere leads to a cooling of this surface layer, with the thickness increasing in time as the cold layer grows downward by diffusion. The thickness of the cold layer grows until a critical value of the Rayleigh number is exceeded. The layer then becomes unstable and sheds filaments of cold fluid into the interior. This flux of buoyancy helps to maintain the turbulence in the well mixed interior. Howard (1966) derived an expression for the time-averaged temperature profile generated by this diffusive growth mechanism, which can be expressed as

$$\frac{T(z) - T_B}{T_S - T_B} = \left(1 + 2\zeta^2\right) \operatorname{erfc} \zeta - 2\pi^{-1/2} \zeta \exp(-\zeta^2). \tag{2}$$

[1] A positive Q corresponds to a net heat flux from the ocean to the atmosphere in our notation. Note that the opposite sign convention is used in some of the previous literature.

The surface temperature is denoted T_S, and T_B is the temperature in the bulk, deep in the mixed layer. The non-dimensional co-ordinate

$$\zeta = -\frac{\sqrt{\pi}}{4}\frac{z}{\delta_c} \tag{3}$$

represents the depth scaled by the conductive lengthscale δ_c. One possibility is to identify the diffusive lengthscale δ_c as the laminar layer thickness in the simplified model shown in figure 1. If the temperature gradient is linear across the surface laminar layer we have

$$T_B - T_S = \frac{Q\delta_c}{\rho c_p \kappa}, \tag{4}$$

so that the bulk-skin temperature difference is determined by the heat flux Q and conductive layer depth δ_c.

In the case of free convection, Saunders (1967) suggested that the conductive lengthscale δ_c and bulk-skin temperature difference, $T_B - T_S$, can be uniquely determined in terms of the heat flux Q by applying the '4/3rds' convection heat transfer law for turbulent Rayleigh-Bénard convection. Scaling theories suggest that

$$\frac{Q}{\rho c_p} = A\kappa \left(\frac{\beta g}{\kappa\nu}\right)^{1/3} \Delta T^{4/3}, \tag{5}$$

for thermal convection of fluid between two isothermal horizontal plates, with the upper surface cooled. The coefficient of thermal expansion is denoted by β, g is the acceleration due to gravity, ν is the kinematic viscosity, $\Delta T = T_B - T_S$ is the temperature difference between the plates and $A = 0.20$ is a constant of proportionality. We can combine (4) and (5) to give

$$\Delta T = A^{-3/4} \left(\frac{Q}{\rho c_p \kappa}\right)^{3/4} \left(\frac{\kappa\nu}{\beta g}\right)^{1/4}, \tag{6}$$

$$\delta_c = A^{-3/4} \left(\frac{Q}{\rho c_p \kappa}\right)^{-1/4} \left(\frac{\kappa\nu}{\beta g}\right)^{1/4}. \tag{7}$$

so that the bulk–skin temperature difference and thermal boundary layer thickness are determined uniquely by the heat flux applied at the surface. In section 4 we will consider how (6) and (7) compare to the corresponding values observed in experiments.

In the ocean, the above picture of the thermal boundary layer is modified due to forced convection generated by wind. Additional shear turbulence is generated by the applied wind stress, acting to reduce the thickness of the laminar-thermal-boundary layer to $\delta_c = \mathcal{O}(1\text{mm})$.

2.2 Modification of surface thermal boundary by straining flow

Osborne (1965) considered the structure of the thermal boundary layer near to the surface in the presence of an applied flow and inferred variations in sea surface temperature due to ocean waves. We discuss this modification to the surface renewal model below and its implication for regions of local upwelling in the ocean.

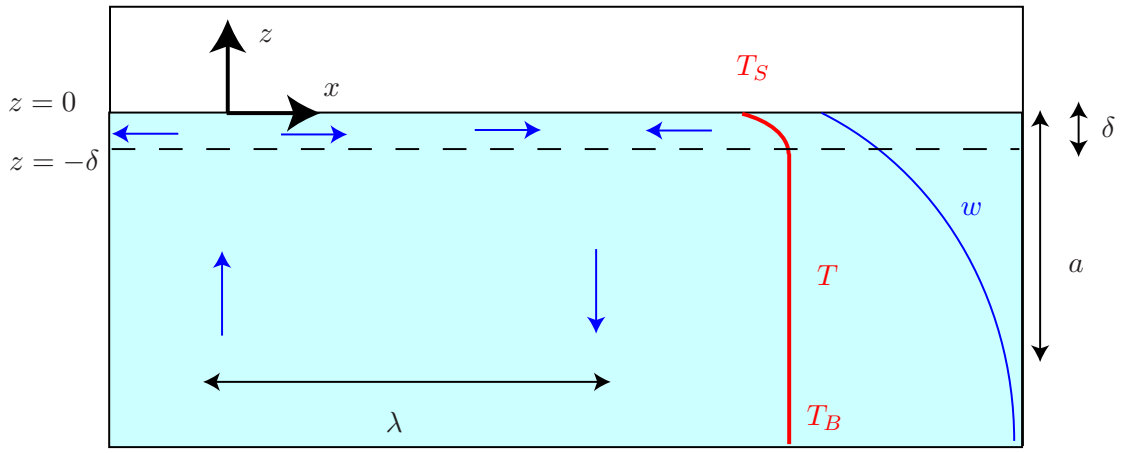

Figure 2: Geometry of the thermal boundary layer in the presence of an imposed internal wave motion. The thermal boundary layer evolves quasi-statically below the free surface, with the internal waves generating diverging and converging flow near to the surface. Typical vertical velocity and temperature profiles are plotted on the right hand side of the figure, with the temperature field varying over a much shorter lengthscale than the velocity field.

Conservation of heat within the fluid is described by the Reynolds-averaged advection-diffusion equation

$$\frac{\partial T}{\partial t} + \mathbf{u} \cdot \nabla T = \kappa \nabla^2 T - \nabla \cdot \left(\overline{\mathbf{u}' T'} \right), \tag{8}$$

where $\overline{(\xi)}$ represents an ensemble average of a variable ξ over a time-scale longer than the typical eddy turnover time-scale but shorter than any time-scale of variation of the bulk flow (see Tennekes & Lumley, 1972, for example.) The ensemble averaged fluid velocity and temperature are denoted by $\mathbf{u}$ and T, while $\mathbf{u}'$ and T' are the corresponding turbulent fluctuations about the mean. We motivate our scalings by considering typical two dimensional ocean internal waves, but the analysis can also be applied to any other system with the same ordering of length-scales (including the axisymmetric flow observed in the laboratory experiments discussed in §3-4). Non-linear internal waves are typically observed to have horizontal wavelengths $\lambda \approx 10 - 100\,\mathrm{m}$, vertical amplitudes $a \approx 1 - 10\,\mathrm{m}$ and frequencies $\omega = \mathcal{O}(0.005)\,\mathrm{Hz}$. The length-scales of variation of the internal wave flow are much larger than the thermal boundary layer thickness (typically $\delta = 0.1 - 1\,\mathrm{cm}$ in the ocean) and so we can make some simplifications to our model under the assumption that $\delta \ll a, \lambda$. Working in a reference frame where the air-water interface is fixed (see figure 2), we expect no normal flow at the free surface so that the vertical velocity $w = 0$ at $z = 0$. We can then approximate the near surface vertical velocity by the leading term in a Taylor expansion

$$w = z \left. \frac{\partial w}{\partial z} \right|_{z=0} + \mathcal{O}\left(a\omega \frac{\delta^2}{a^2} \right). \tag{9}$$

Continuity requires that the local upwelling be accompanied by a horizontally diverging flow. We can think of the internal waves generating a local straining flow about some point

within the thermal boundary layer, so that

$$w = -\alpha z, \qquad u = \alpha_1 x, \qquad v = \alpha_2 y, \qquad \alpha = \alpha_1 + \alpha_2 \tag{10}$$

where $\alpha = \mathcal{O}(\omega)$ is the vertical strain rate, (x, y) are the horizontal co-ordinates relative to the centre of the divergence, and (u, v) are the corresponding horizontal components of velocity. We expect horizontal variations to scale with the flow wavelength λ and vertical variations to scale with the boundary layer thickness δ, so that $\partial_x, \partial_y \ll \partial_z$ and we can neglect horizontal diffusion compared to vertical diffusion across the boundary layer. If Q is independent of x and y, we expect horizontal variations in temperature to be small compared to the bulk skin temperature difference, so that $\mathbf{u} \cdot \nabla T \approx w \partial_z T$. Finally, we assume that turbulence is suppressed near to the surface, so that $\overline{\mathbf{u}'T'} \approx 0$ in the upper laminar layer $-\delta < z < 0$. The heat equation (8) then simplifies to give

$$\frac{\partial T}{\partial t} - \alpha z \frac{\partial T}{\partial z} = \kappa \frac{\partial^2 T}{\partial z^2}. \tag{11}$$

For near surface flow generated by internal waves we expect the time dependent term to be comparable to the vertical advection (since $\alpha < \omega$ for linear internal waves). This possibility was discussed in more detail by Osborne (1965), with the resulting solutions exhibiting a wave-like propagation of the temperature signal through the boundary layer. We will focus on the quasi-steady case relevant to our laboratory experiments, so that (11) reduces to the ordinary differential equation

$$-\alpha z \frac{\partial T}{\partial z} = \kappa \frac{\partial^2 T}{\partial z^2}. \tag{12}$$

This is subject to boundary conditions

$$T = T_B \quad \text{at} \quad z = -\delta, \qquad -\rho c_p \kappa \frac{\partial T}{\partial z} = Q \quad \text{at} \quad z = 0, \tag{13}$$

so that the temperature matches the bulk temperature at the top of the mixed layer and is subject to an imposed heat flux at the atmosphere-ocean interface. The system (12–13) has solution

$$T(z) - T_B = \frac{Q}{\rho c_p \kappa} \int_{-\delta}^{z} \exp\left(-\frac{\alpha \xi^2}{2\kappa}\right) d\xi, \tag{14}$$

so that we observe a bulk–skin temperature difference

$$T_S - T_B = \frac{Q}{\rho c_p \kappa} \int_{-\delta}^{0} \exp\left(-\frac{\alpha \xi^2}{2\kappa}\right) d\xi. \tag{15}$$

As α varies we obtain different asymptotic limits. In the limit of no imposed flow ($\alpha = 0$) we recover the linear conduction temperature difference

$$T_S - T_B = \frac{Q\delta}{\rho c_p \kappa}. \tag{16}$$

For flows with large strain rate,

$$\frac{\alpha \delta^2}{\kappa} \gg 1, \tag{17}$$

we obtain a temperature difference

$$T_S - T_B = \frac{Q}{\rho c_p}\sqrt{\frac{\pi}{2\kappa\alpha}}. \tag{18}$$

We note that the equation (18) closely resembles the prediction of Leighton *et al.* (2003), who used a surface straining model to describe the static free convection boundary layer (with $\alpha = 0$ in our notation.) The Leighton *et al.* (2003) model assumes that, for free convection, the thermal boundary layer is set up by a balance between vertical diffusion and a flow with strain rate γ, generated by turbulence in the interior. Leighton *et al.* (2003) suggest that their result can also be generalised for other sources of turbulence by a suitable choice of the effective strain rate γ. It is interesting to note that the large strain rate limit (18) of the Osborne (1965) theory agrees with the Leighton *et al.* (2003) result if we take $\gamma = \alpha$, corresponding to the imposed vertical advection dominating that generated by convective turbulence.

2.3 Non-dimensional formulation

We can also describe the bulk-skin temperature difference in non-dimensional form, in order to identify the different dynamical balances that can be observed in the thermal boundary layer, and ascertain when each balance can be applied. Scaling vertical lengths with δ, temperature differences with the conductive temperature difference $Q\delta/\rho c_p\kappa$, and time with $1/\omega$, we define non-dimensional variables $\hat{z} = z/\delta$, $\theta = \rho c_p\kappa(T - T_B)/Q\delta$ and $\hat{t} = \omega t$. The governing equation (11) becomes

$$\mathrm{St}\,\mathrm{Pe}\,\frac{\partial\theta}{\partial\hat{t}} - \mathrm{Pe}\,\hat{z}\frac{\partial\theta}{\partial\hat{z}} = \frac{\partial^2\theta}{\partial\hat{z}^2}, \tag{19}$$

where the *Péclet number*

$$\mathrm{Pe} = \frac{\alpha\delta^2}{\kappa}, \tag{20}$$

measures the importance of advection of heat relative to diffusion, and the *Strouhal* number,

$$\mathrm{St} = \frac{\omega}{\alpha}, \tag{21}$$

is the dimensionless frequency of the wave motion. The non-dimensional forms of the boundary conditions (13) are

$$\theta = 0 \quad \text{at} \quad \hat{z} = -1, \qquad \text{and} \qquad \frac{\partial\theta}{\partial\hat{z}} = -1 \quad \text{at} \quad \hat{z} = 0. \tag{22}$$

We immediately see from (19) that we can only neglect the unsteady term if $\mathrm{St} \ll 1$ and we have a low frequency motion. Linear internal and surface waves have $\alpha < \omega$, so that $\mathrm{St} > 1$ and the unsteady term must be retained.

For steady flows, the Osborne (1965) prediction (15) can be rewritten as

$$\frac{1}{\mathrm{Nu}} = \sqrt{\frac{\pi}{2}}\frac{\mathrm{erf}\left[(\mathrm{Pe}/2)^{1/2}\right]}{\mathrm{Pe}^{1/2}}, \tag{23}$$

where the *Nusselt number*

$$\mathrm{Nu} = \frac{Q\delta}{\rho c_p \kappa \left(T_S - T_B\right)}, \tag{24}$$

represents the ratio of total heat flux compared to the conducted heat flux for the static ($\alpha = 0$) boundary layer. We have used the error function

$$\mathrm{erf}\left[x\right] = \frac{2}{\sqrt{\pi}} \int_0^x \exp\left(-u^2\right)\, du \tag{25}$$

here. For large Péclet number (23) reduces to

$$\frac{1}{\mathrm{Nu}} \sim \sqrt{\frac{\pi}{2\,\mathrm{Pe}}} \quad \text{as} \quad \mathrm{Pe} \to \infty, \tag{26}$$

so that the limit (18) is valid whenever $\mathrm{Pe} = \alpha\delta^2/\kappa \gg 1$. For small Péclet number ($\mathrm{Pe} \ll 1$) we have

$$\frac{1}{\mathrm{Nu}} = 1 - \frac{\mathrm{Pe}}{6} + \mathcal{O}\left(\mathrm{Pe}^2\right). \tag{27}$$

We will see that this limit has important consequences later on.

In §3 and §4 we discuss an experimental investigation of the dynamics described by this theory.

3 Experimental Procedure

A laboratory experiment was used to investigate the structure of the thermal boundary layer below a free surface. The experimental set up is shown in figures 3 and 4 A laminar jet was created at the base of an inner tank by pumping fluid through a vertical nozzle. The nozzle was covered by a sponge to generate a diffuse source of momentum, thus allowing the generation of small strain rates close to the free surface. The pump flow rate was varied between $0.12\,\mathrm{cm}^3\,\mathrm{s}^{-1} \leq F \leq 1.14\,\mathrm{cm}^3\,\mathrm{s}^{-1}$, in order to alter the input momentum flux and hence the strain rate close to the surface. The jet decelerates as it approaches the free surface, so that there is an axisymmetric straining flow close to the surface (indicated by the blue arrows in figure 4). The fluid then spreads radially, creating a surface divergence, before overflowing into an outer tank where fluid is returned to the pump via a sink. The outer tank has insulated side walls and bottom so that the dominant heat loss is across the air–water interface.

The bulk temperature was measured with a resolution of 0.02°C by a digital HOBO data logging thermometer placed deep in the tank. A PME microscale temperature–conductivity (T-C) probe (incorporating a Thermometrics FP07 thermistor) was lowered into the tank from above in order to measure the variation of temperature with depth and enable estimation of the skin layer thickness δ. The probe tip was aligned to pierce the interface close to the centre of the upwelling jet. Temperature profile measurements were taken over the upper 5 cm of the tank interior, with one sample taken every 0.001 cm. Downward sampling was used so that the probe tip could take measurements before the probe casing influenced the upwelling flow. Several measurements were also made with an upward moving U–shaped probe for the static thermal boundary layer case ($\alpha = 0$), and no qualitative

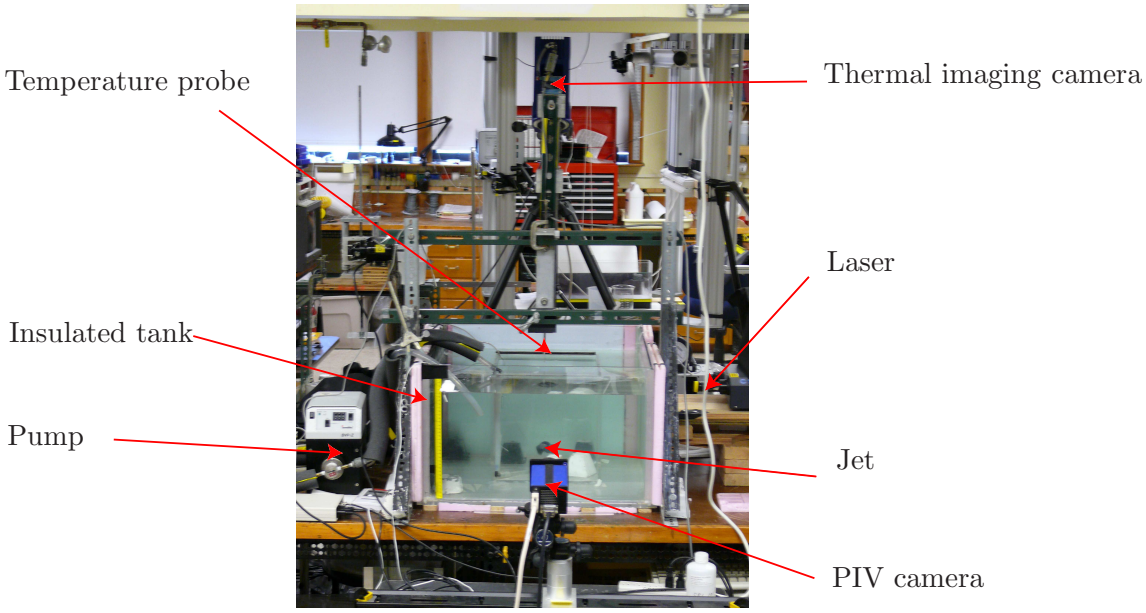

Figure 3: Photograph of the experimental apparatus.

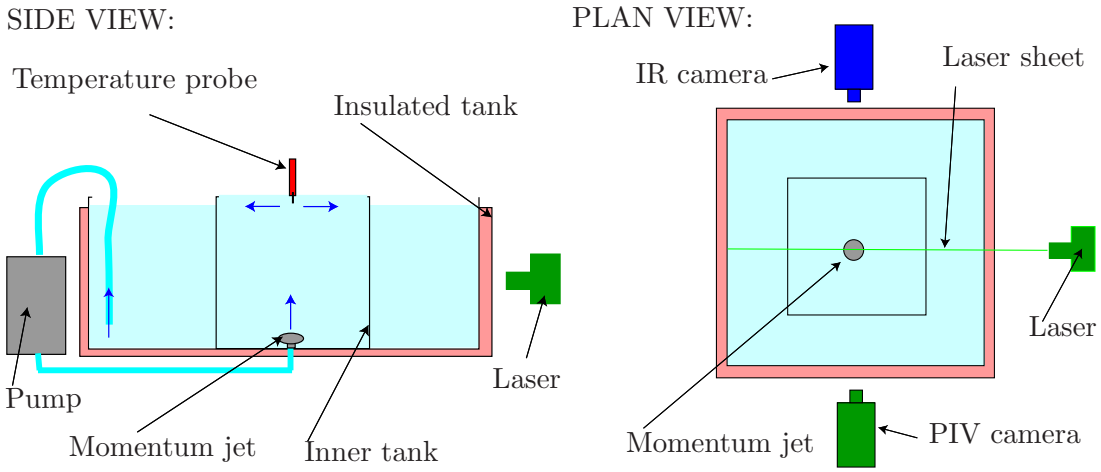

Figure 4: Schematic diagram illustrating the experimental set-up. Fluid is injected via a jet at the base of the inner tank to create a near surface flow divergence, as indicated by the blue arrows.

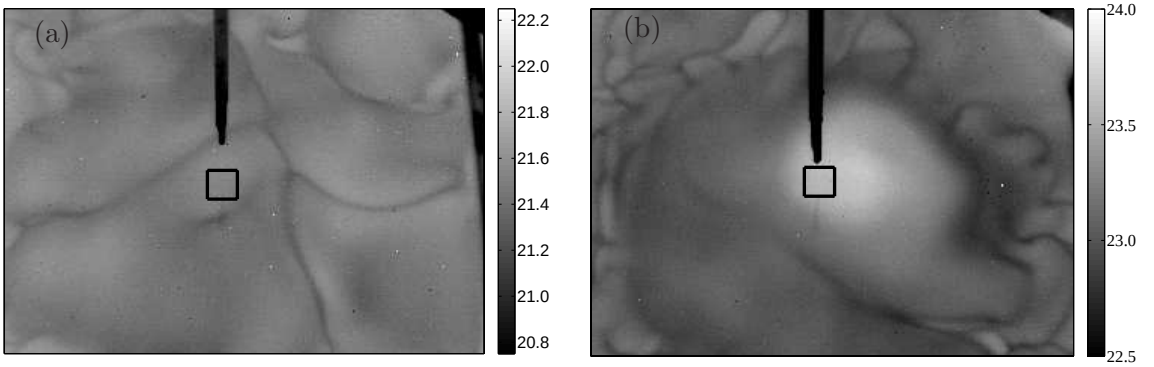

Figure 5: Instantaneous images of the measured temperature, in °C, at the free surface, for (a) pure free convection and (b) an upwelling jet of volume flux $F = 1.14\,\mathrm{cm}^3\,\mathrm{s}^{-1}$. Each image shows a region of the surface 15 cm × 12 cm, with the 1 cm × 1 cm averaging region indicated by a black outline. The microscale-temperature probe shows in black at the centre of the image, shortly before it is lowered into the water. Convection roll structures are observed in the free convective case (a) with cold regions above local regions of downwelling. The relatively warm patch in the centre of frame (b) corresponds to the thermal signature of the upwelling jet. Note that the temperature scales differ for each image, since the bulk temperature T_B differs between the images.

difference in temperature profiles was observed. This suggests that the vertical motion of the probe tip does not have a strong influence on the thermal boundary layer, as similar profiles are observed for both an upward and downward moving probe. The analogue output of the microscale conductivity probes was subject to some contamination by electrical noise generated within the laboratory. This noise implies an accuracy of only 0.1°C in the temperature profile measurements.

The free surface temperature was measured to an accuracy of 0.001°C and at a sample rate of 20 Hz with an infra-red thermal imaging camera, mounted 60cm above the water surface with a viewing angle of 26° to the vertical. In particular, the free surface temperature was determined by a spatial average over a $1\,\mathrm{cm}^2$ square box centred on the T-C probe tip, and then a further time average over 5 seconds worth of images. Single images of the free surface temperature variation are shown in figure 5, both with and without an imposed flow, with the measurement region marked by a black outline.

The velocity field was measured using a particle image velocimetry technique, which is briefly described below. The tank was seeded with 10 μm diameter glass beads of near neutral buoyancy, which were illuminated by a vertical laser sheet passing through the centre-plane of the jet. The particles effectively behave as passive tracers for the flow speeds of $\mathcal{O}(1\,\mathrm{cm/s})$ observed in the jet. The particle displacements between a pair of consecutive camera frames are then correlated to estimate the velocity components in the plane of illumination. An interval of 0.06 s between frames was found to give best resolution of the flow. For each flow rate, a sequence of 155 image pairs was taken at a sampling rate of 4 Hz. This sequence was then time averaged and a subsequent mean vertical velocity profile $w(z)$ was then calculated for the centre of the jet. For each value of z a horizontal average of w was taken across a cross-section of width 2 cm about the centreline of the jet.

An integral heat budget was used to estimate the total heat flux across the air-water interface. If we assume negligible heat loss across the well insulated side walls and bottom of the tank then most of the heat loss has to occur across the free surface. Turbulent convection maintains the interior of the tank at a uniform temperature, except in the small thermal boundary layer over the upper centimetre of depth. The order 1 cm surface boundary layer comprises less than 5% of the 30 cm depth of the tank, and so we neglect the small effect of departure from the bulk temperature in this thermal boundary layer. Balancing the rate of change of heat within the tank to the heat flux across the free surface, we obtain

$$\rho c_p \frac{d}{dt}\left(\mathcal{V} T_B\right) = \mathcal{A} Q, \tag{28}$$

where $\mathcal{V}$ is the volume of water in the tank, and $\mathcal{A}$ is the area of the free surface. Note that we have assumed that the water-air heat flux Q is relatively uniformly distributed across the free surface. The integral heat budget (28) gives an estimate of the water–air heat flux Q from the temporal variation of the bulk temperature measured with the HOBO digital thermometer. The time rate of change of T_B was calculated by applying a 600 second box filter to the temperature record to remove noise, and then using the difference in smoothed temperature 300 seconds before and 300 seconds after each measurement to calculate the derivative. This provided a smooth variation of heat flux in time.

The above measurements were taken for different strain rates (i.e different flow rates F) and also different bulk temperatures. For each experiment, the following procedure was adopted. One hundred thermal camera images were taken over a period of 5 seconds, before a temperature–depth profile was taken with the T-C probe moving downward through the free surface. The heat flux and bulk temperature values were recorded continuously during several experiments. Particle image velocimetry measurements were taken for each flow rate for a range of bulk temperatures. It was found that there was negligible change in the near surface strain rate α with bulk temperature, suggesting that the dynamical effect of convection is relatively weak compared to that of the imposed flow of the jet. A single average value of α was therefore used for each flow rate in the subsequent calculations.

4 Experimental results

A series of measurements were taken to assess the accuracy of the method and explore how an applied upwelling flow alters the thermal boundary layer structure. In §4.1 we present measurements of the thermal boundary layer for pure convection with no imposed flow in order to provide a consistency check on our results. We then move on to consider the effects of an imposed upwelling flow in §4.2, before giving a qualitative discussion of the effects of downwelling flow and the presence of surfactants in §4.3.

4.1 Convective boundary layer with no imposed flow

The experimental procedure was first tested by taking measurements of a purely convective thermal boundary layer as a consistency check with previous studies (Howard, 1966; Katsaros *et al.*, 1977). Figure 6 shows the raw output from a typical measured sub-surface temperature profile. The persistent variation of 0.1°C might be explained in part by elec-

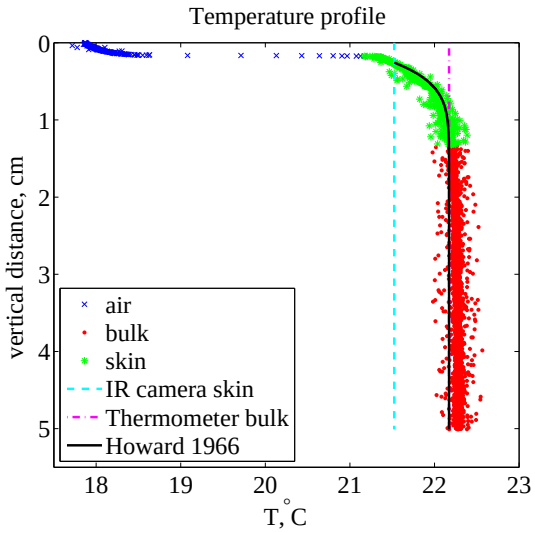

Figure 6: Variation in sub-surface temperature in °C with depth in cm. The measured temperature signal at each point is shown by symbols, with blue cross symbols denoting measurements in air, green star symbols denoting measurements in the skin layer and red dot symbols denoting measurements in the interior as determined by an automated algorithm (see text). The independent thermal camera measurement of the surface temperature is shown by a dashed blue line and the thermometer measurement of the bulk temperature is shown by a dash-dotted pink line. The solid black curve shows the profile predicted by the Howard (1966) convective boundary layer theory using $\zeta = -\sqrt{\pi}z/4\delta_c$.

trical noise in the laboratory contaminating the signal.

An automated algorithm was used to determine the vertical position of the air–water interface and also to determine the depth of the skin layer. Measurements in approximately the upper 0.3 cm have been taken in air (blue cross symbols) and are shown purely to illustrate the surface detection algorithm (the instrument does not measure temperature accurately in air.) The transition from readings taken in air to readings taken in water was characterised by a region of large vertical gradient in the temperature signal, as the probe pierced the interface. The position of the air-water interface was therefore estimated by taking the vertical co-ordinate of the tenth data point after the maximum value of dT/dz was attained. This algorithm systematically under-predicts the surface temperature compared to the thermal camera measurement, due in part to the effects of partial immersion of the probe tip and surface tension dominated deformation of the interface. However, the temperature profile reaches the same value as the thermal camera estimate of surface temperature within 0.05 cm (which is, perhaps not coincidentally, about the diameter of the glass encased thermistor). Hence, the disagreement in surface temperature between the temperature profile and the thermal camera has only a small effect on the inferred values of the thermal boundary layer thickness $\delta = \mathcal{O}(1\,\mathrm{cm})$. The remaining data points in the temperature profile were then inferred to be in the skin layer (green star symbols) if the observed temperature deviated from the average bulk temperature by more than 5% of the bulk–skin temperature difference (where the bulk temperature was taken from the temperature profile at 4 cm depth.) The data points from the remainder of the profile in the interior are plotted using red circles. This algorithm enabled an estimate of the thermal boundary layer thickness δ by computing the depth of the inferred skin layer. Typically observed values lie in the range $0.4\,\mathrm{cm} \leq \delta \leq 1.5\,\mathrm{cm}$, as expected, with thinner boundary layers observed for a larger surface heat flux. The theoretical solution (2) due to Howard (1966) is also plotted in figure 6 (solid black curve), and shows good agreement with the observed shape of the temperature profile. Note that we have estimated the conductive lengthscale δ_c using (7) here.

Figure 7 shows a comparison of the observed bulk–skin temperature difference $T_B - T_S$ with the prediction (6) made by applying the '4/3rds' heat flux law. We observe a linear relationship between the observed and predicted bulk-skin temperature differences, with equation (6) under-predicting the observed bulk-skin temperature difference by approximately 0.3°C. The cause of this offset was not immediately clear, but is of a consistent order of magnitude to the bulk-skin temperature differences that can be generated by Marangoni convection (Katsaros, 1980). The surface may also be affected by contamination with surfactants either contained within the tap water used, or those that have settled onto the surface from the atmosphere. We note that some intrinsic scatter in the data is to be expected due to turbulent flow fluctuations. The convection theory described in §2.1 is based on a statistically steady state approximation, with the governing equations averaged both in time and horizontal space. This means that some time-dependent and spatial variation is expected between individual temperature profiles (in particular we expect some horizontal variation in temperature due to the structure of the convection cells). The above results and their agreement with previous theories give us confidence that our experimental techniques are adequate before moving on to consider the effect of an upwelling flow on the thermal boundary layer dynamics.

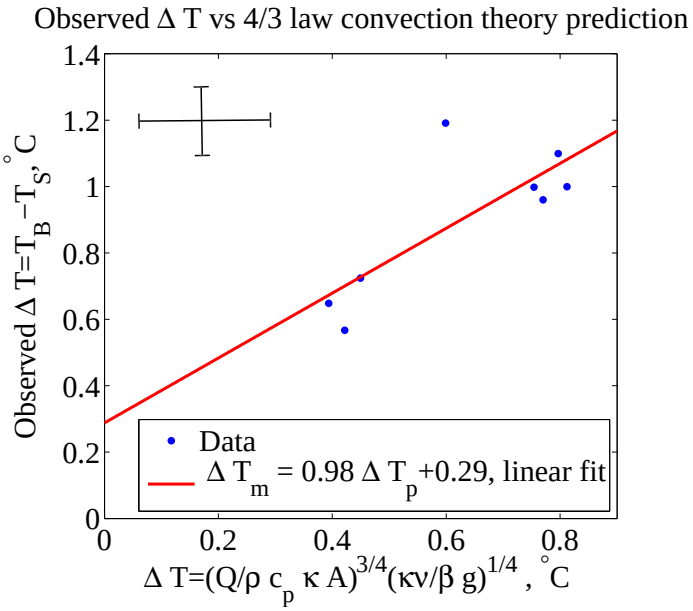

Figure 7: Comparison of the observed bulk–skin temperature (measured using thermal camera and digital thermometer) with the theoretical prediction $T_B - T_S = A^{-3/4}\,(Q/\rho c_p \kappa)^{3/4}\,(\kappa\nu/\beta g)^{1/4}$ given by (6). The red curve shows a linear fit to the relationship between measured values ΔT_m and predicted values ΔT_p. Typical error bars are shown by the cross in the top left corner.

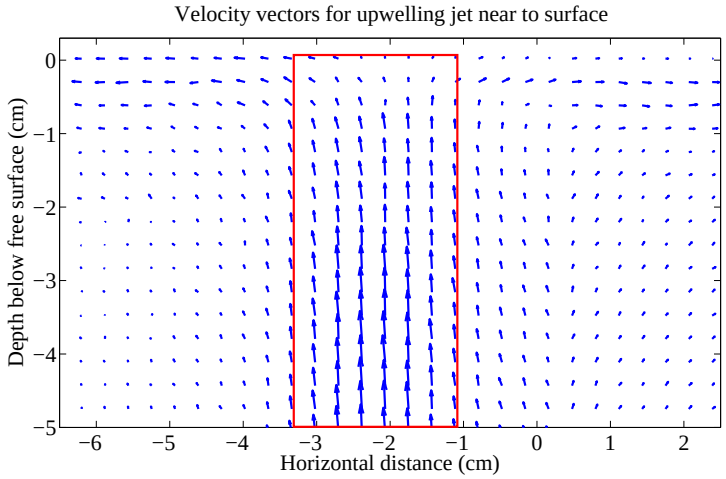

Figure 8: Time-averaged velocity vectors calculated from particle image velocimetry measurements for a laminar momentum jet with volume flux $F = 1.14\,\mathrm{cm}^3\,\mathrm{s}^{-1}$. The vertical jet exerts a local upwelling between $x = -3.2\,\mathrm{cm}$ and $x = -1.2\,\mathrm{cm}$, generating a diverging flow near to the surface. The mean vertical velocity is determined by taking a cross sectional average at each height z within the red rectangle.

4.2 Convective boundary layer with imposed near surface divergence

A near surface divergence was generated by the local upwelling flow produced by the diffuse vertical jet described in §3. The jet was of laminar character, and remained relatively steady over the period of an experiment, with occasional intermittent bursts of unsteadiness. Figure 8 shows a plot of the time averaged flow vectors measured using particle image velocimetry for a jet with volume flux $F = 1.14\,\mathrm{cm}^3\,\mathrm{s}^{-1}$. The jet has a confined core flowing upwards with weak entrainment of the exterior fluid. The flow diverges radially as the free surface is approached. Figure 9 shows a plot of the average vertical velocity $w(z)$ near the centre of the jet, calculated using the methods described in §3. Directly above the source ($z \sim -20\,\mathrm{cm}$) we observe an increase in vertical velocity - this effect is a consequence of the plane of measurement not coinciding precisely with the centre of the jet. Closer to the surface we observe the expected vertical deceleration, with the vertical velocity tending to zero as we approach the free surface. The variation of vertical velocity w is approximately linear in z over the upper 2.5 cm of the profile. This lengthscale exceeds the typical thickness of the thermal boundary layer $\delta = \mathcal{O}(1\,\mathrm{cm})$, so that we are in a regime of constant strain rate within the thermal boundary layer. We estimate the constant strain rate α by applying a linear finite difference across the upper 2 cm of the profile, so that

$$\alpha = \frac{w(z = 0\,\mathrm{cm}) - w(z = -2\,\mathrm{cm})}{2\,\mathrm{cm}}. \tag{29}$$

Different values of α were obtained by varying the jet flow rate - these are are summarised in table 1.

The imposed diverging flow field has a significant effect on the temperatures observed both at and below the free surface. Figure 5 shows an example of the instantaneous free surface temperature measured with the infra-red thermal camera, for cases with and without

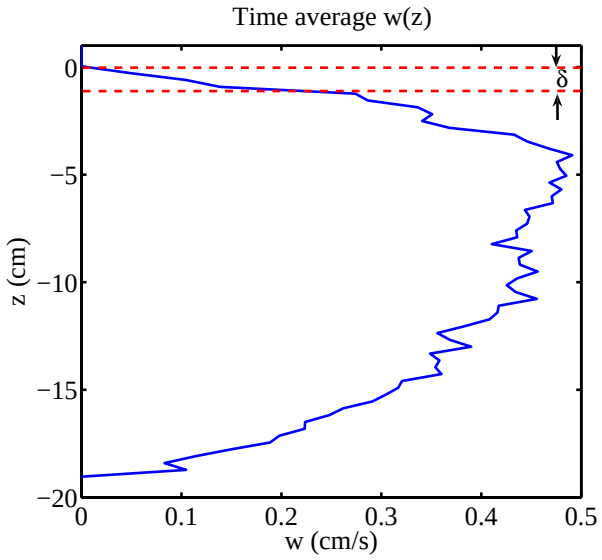

Figure 9: Typical variation of mean vertical velocity w with depth z, for a jet with volume flux $F = 1.14\,\mathrm{cm}^3\,\mathrm{s}^{-1}$. The velocity variation is linear close to the surface, so that the strain rate is approximately constant over the width of the thermal boundary layer δ. A typical reference value of δ is marked by red dashed lines for comparison.

Flow rate F ($\mathrm{cm}^3\,\mathrm{s}^{-1}$)	0.12	0.19	0.60	1.14
Strain rate α (s^{-1})	0.043	0.057	0.118	0.158

Table 1: Values of near surface strain rate $\alpha = \partial w/\partial z$ estimated from particle image velocimetry measurements.

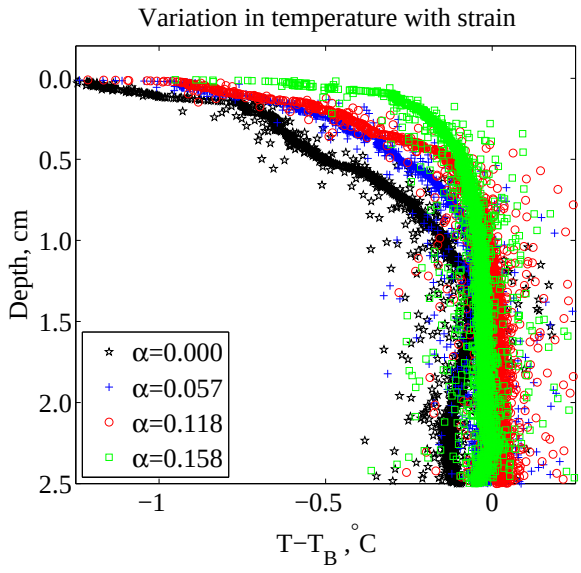

Figure 10: Variation of sub-surface temperature from bulk temperature, $T - T_B$, with depth z, for different values of the applied strain rate $\alpha = \partial w/\partial z$. As α, and hence the vertical advection, increases the boundary layer becomes thinner, and the bulk skin temperature difference is reduced.

an imposed flow. With no imposed flow (figure 5(a)) we observe regions of warm temperature bounded by bands of colder fluid. These patches are due to convection cells, with upwelling creating a warm region at their centre and downwelling at the cell boundaries creating a colder surface temperature. These structures bear a striking resemblance with those observed in the DNS of Leighton *et al.* (2003) (see their figure 2), and provide a qualitative indication that vertical sub-surface flow influences the surface temperature.

The addition of a vertical jet flow produces an obvious change in the free surface temperature pattern, as seen in figure 5(b). Upwelling of heat from the interior leads to a localised patch of warmer surface temperature above the centre of the jet, as compared to the surface temperature in the far field. The convection cell structure appears to be suppressed within this patch. This may reflect the fact that the jet creates a relatively large Péclet number in the boundary layer ($\mathrm{Pe} = \alpha\delta^2/\kappa \approx 10 - 100$). The convection cell structures are set up by a diffusive balance across an upper conductive layer. For large Péclet number the advection of heat by the jet dominates over diffusion and so the convection cell structures are suppressed. A quantitative analysis of the thermal boundary layer is discussed below.

The variation in surface temperature is accompanied by a corresponding change to the sub-surface thermal boundary layer. Figure 10 shows the measured temperature variation with depth for four different applied strain rates. The measurements suggest that the bulk-skin temperature difference is reduced as the strain rate increases. This is qualitatively consistent with the Osborne (1965) theory, with the surface temperature being locally larger due to vertical advection of warm fluid from the interior. We also note a reduction in the measured boundary layer thickness δ as we increase the strain rate α, with the temperature variation confined to a narrower region close to the surface.

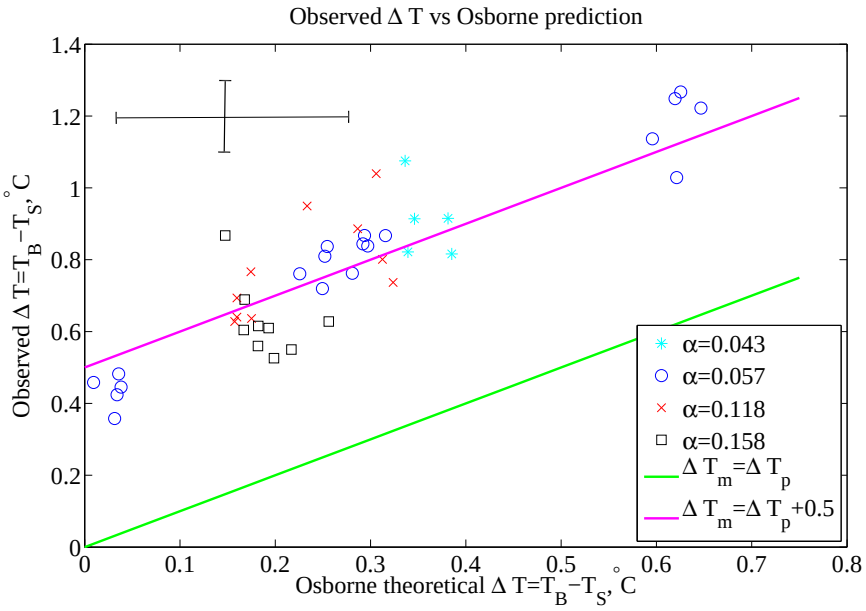

Figure 11: Comparison of observed bulk-skin temperature difference in °C, to the Osborne (1965) theoretical prediction (15). The observed surface temperature is measured using the thermal imaging camera, and the bulk temperature is measured by the digital thermometer. Also shown are the lines $\Delta T_{measured} = \Delta T_{predicted}$ and $\Delta T_{measured} = \Delta T_{predicted} + 0.5$°C for reference. The cross in the top left corner shows the typical scale of errors inferred from experimental measurement precision.

In order to provide a quantitative comparison with the Osborne (1965) theory, the measured values of α, δ and Q were used to predict a value of the bulk-skin temperature difference for each experiment according to (15). Figure 11 shows the predicted bulk-skin temperature difference compared to the value measured using the infra-red camera and digital thermometer readings for each individual experiment. The results follow a linear trend, with the Osborne (1965) prediction (15) producing a consistent under-estimate of the observed bulk-skin temperature difference by approximately 0.5°C. We again note that we expect some intrinsic scatter in the data as a result of time dependent turbulent flow fluctuations. The Osborne (1965) theory is derived for a statistically steady state, described by a surface renewal type theory for the convective boundary layer. This means that some time-dependent variation is expected between individual temperature profiles as filaments of cold fluid detach from the boundary layer and mix downwards. The level of scatter is also of a similar magnitude to the error estimates provided by a compound of the measurement precision of each of the instruments, as shown by the error bars in figure 11. The cause of the consistent offset of 0.5°C was again undetermined, but may also be consistent with the effects of Marangoni convection or surface contamination.

An alternative comparison with the Osborne (1965) theory is to consider the measured variation of the non-dimensional Nusselt number Nu with the Péclet number Pe, as shown on logarithmic scales in figure 12. The data appear to follow the scaling of the large Péclet

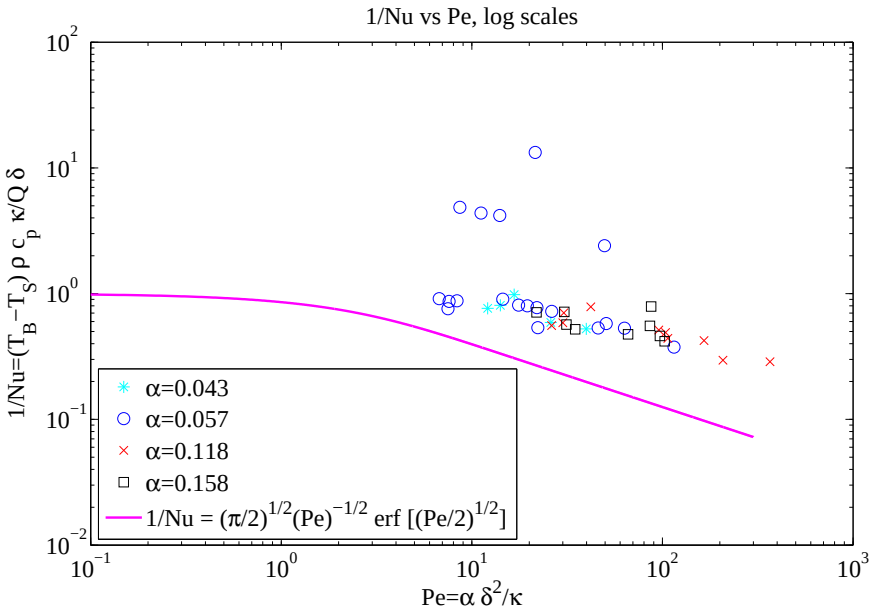

Figure 12: Variation of inverse Nusselt number $1/\mathrm{Nu} = (T_B - T_S)\rho c_p \kappa / Q\delta$ with Péclet number $\mathrm{Pe} = \alpha\delta^2/\kappa$, plotted on logarithmic scales. The non-dimensional form of the Osborne (1965) prediction (23) is plotted with a solid line for comparison.

number limit, with

$$\frac{1}{\mathrm{Nu}} \sim \sqrt{\frac{\pi}{2}}\mathrm{Pe}^{-1/2}, \qquad \text{as} \qquad \mathrm{Pe} \to \infty. \tag{30}$$

This suggests that the Osborne (1965) theory provides an effective description of large Péclet number flow in the laboratory.

4.3 Discussion of surface convergence and surfactant effects

Attempts were made to perform experiments with a converging flow generated close to the surface. In order to generate a converging flow the direction of the pump was reversed so as to create a sink flow in the inner tank. In addition the sink nozzle was moved to within 3 cm of the surface to allow large strain rates to be observed close to the interface. Figure 13 shows the surface temperature measured for a strong sink flow of volume flux $F = 90\,\mathrm{cm}^3\,\mathrm{s}^{-1}$. This set up did not allow detailed quantitative measurements, as we could not obtain a constant strain rate α over the entire width of the thermal boundary layer. However, a reduction in surface temperature of approximately 0.2°C was observed in the neighbourhood of the draining sink flow.

Ten experiments were also performed with an insoluble surfactant added to the water in order to investigate the effects of contamination by a surface film. 250μl of cholesterol was added to the surface of the tank, the tank was stirred and left to settle for 30 minutes. Figure 14 shows a comparison of predicted and observed values of the bulk-skin temperature difference both without and with the addition of artificial surfactant. The addition of surfactant generates a reduction in the observed bulk-skin temperature difference, so that

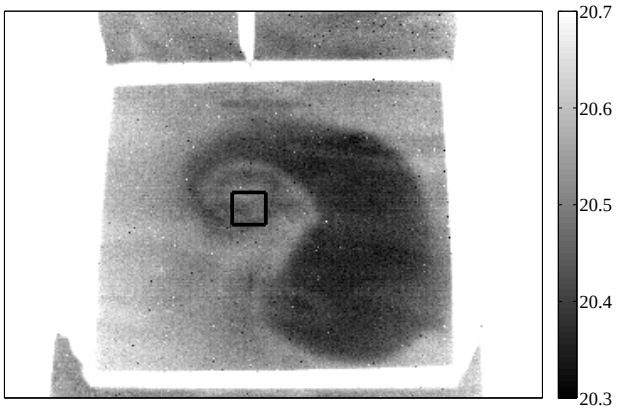

Figure 13: Surface temperature measured in the presence of a strong sink flow of volume flux $F = 90\,\mathrm{cm}^3\,\mathrm{s}^{-1}$. The cold (dark) region is observed above regions of near-surface convergence generated by the sink flow draining the container. The cause of the warm patch close to the sink is undetermined, but suggests that horizontal advection may be important in this flow.

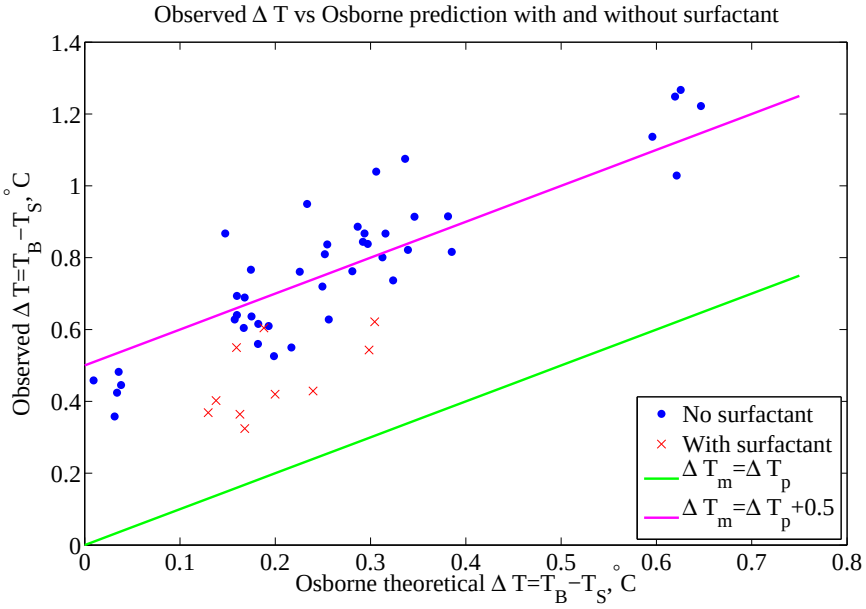

Figure 14: Comparison of observed bulk-skin temperature difference in °C, to the Osborne (1965) theoretical prediction (15). Data without the addition of artificial surfactant are plotted with blue points and measurements with the addition of surfactant are plotted with red crosses.

the skin temperature is warmer than we would find without the presence of surfactant. This increase in surface temperature is somewhat surprising, appearing to oppose the usually quoted effect of a surface film (e.g. McKenna & McGillis, 2004). The observed strain rate appears to be significantly reduced by the addition of surfactant, with a change in strain rate from $\alpha = 0.43\,\mathrm{s}^{-1}$ to $\alpha = 0.27\,\mathrm{s}^{-1}$. This is consistent with the expected effect of adding surfactant, as the increase in interfacial tension generates a stress acting to oppose the radially diverging flow and hence reduce near surface fluid velocity (McKenna & McGillis, 2004).

5 Discussion

The laboratory results presented above demonstrate that an imposed near surface diverging flow can generate local variations in the temperature at the free surface. The Osborne (1965) model effectively describes the trends observed in the laboratory experiments at large Péclet number, although it appears to under-predict the observed bulk-skin temperature difference by an offset of approximately 0.5°C. In a large Péclet number regime, the Osborne (1965) theoretical prediction (15) reduces to the limit (18). This limit has the interesting feature that the bulk-skin temperature difference is independent of the boundary layer thickness. The vertical heat transport from the interior is dominated by advection, and so the free surface temperature is controlled by a steady-state balance between vertical advection of heat into the boundary layer and loss of heat into the atmosphere. The thermal boundary layer then adjusts its thickness so that it supplies the necessary conducted heat flux at the air-water interface.

The cause of the 0.5°C offset is undetermined, but could be due to processes such as Marangoni-Bénard convection. Further investigation is required in order to explain this behaviour.

We conclude with a discussion of the application to oceanic flows. The laboratory experiments principally explored a regime of large Péclet number, where the advection of heat dominates diffusion over most of the thermal boundary layer. We expect ocean internal waves to produce flows with much smaller Péclet numbers, since oceanic turbulence generated by a surface wind stress acts to reduce the thermal boundary layer thickness. If we take a typical strain rate of $\alpha = 0.002\,\mathrm{s}^{-1}$ (Gasparovic *et al.*, 1988), a thermal conductivity $\kappa \approx 0.001\,\mathrm{cm}^2\,\mathrm{s}^{-1}$ and an ocean skin layer thickness of $\delta \approx 0.1\,\mathrm{cm}$ (Saunders, 1967) we obtain $\mathrm{Pe} = 0.02$. In the small Péclet number regime we can no longer apply the limit (18), with diffusion playing a more important role in the thermodynamical balance close to the air-water interface. We then expect the bulk-skin temperature difference to have a strong dependence on the thermal boundary layer thickness. Attaining a small Péclet number regime was beyond the scope of the current experimental set up, and so further experimental work is needed in order to explore this limit. In addition, internal waves are an inherently unsteady phenomenon. As previously discussed, the Strouhal number $\mathrm{St} = \omega/\alpha > 1$, and so we cannot use asymptotic arguments to neglect time-dependent variation in the heat equation (8). Osborne (1965) treats linearised time-dependent solutions in three different scenarios, corresponding to different hypotheses as to how the skin layer thickness and bulk temperature respond to the action of waves. Further work is required to determine which, if any, of these cases is appropriate for application to internal wave modulation of the sea

surface temperature.

Having determined that localised flow structures can influence temperature at an air-water interface, it is natural to ask whether such flows have significant impact on ocean to atmosphere heat and gas exchange. For the case of internal waves we present a simplified model calculation, under the (slightly unrealistic) assumption that the steady Osborne (1965) result can be applied in a quasi-steady fashion. We expect internal waves to generate alternating periods of diverging and converging flow near to the free surface. As a simplified model, we pose that the internal waves generate a time-dependent strain $\alpha = \alpha_0 \cos \omega t$ near to the ocean free surface. If we assume that the boundary layer evolves in a quasi-steady fashion, with constant skin layer thickness δ, we can apply the Osborne (1965) result (15) to predict the bulk-skin temperature difference at each time t. The equation (15) is highly asymmetric as we vary α between positive and negative values, and so we might expect a significant difference between the time averaged skin temperature in the presence of waves, and that obtained in a calm ocean with $\alpha = 0$. Using a typical ocean skin layer thickness of $\delta = 0.1\,\mathrm{cm}$, ocean–atmosphere heat flux of $Q = 100\,\mathrm{W\,m^{-2}}$ and internal wave strain rate of $\alpha_0 = 0.002\,\mathrm{s^{-1}}$ we obtain a time averaged bulk-skin temperature difference of $\overline{\Delta T} = 0.1671^\circ\mathrm{C}$. Interestingly, this does not differ significantly from the static bulk-skin temperature difference of $\Delta T = 0.1667^\circ\mathrm{C}$ for $\alpha = 0$. This result is initially surprising, but can be reconciled by considering the small Pe expansion of the non-dimensional result (23). Recall, that for $\mathrm{Pe} \ll 1$, (27) gives

$$\frac{1}{\mathrm{Nu}} = 1 - \frac{\mathrm{Pe}}{6} + \mathcal{O}\left(\mathrm{Pe}^2\right). \tag{31}$$

This implies that small Péclet number flows can only induce small changes in the bulk-skin temperature difference, with the change from the static bulk-skin temperature difference only at $\mathcal{O}\left(\mathrm{Pe}\right)$. The Péclet number relevant to our internal wave example is $\mathrm{Pe} = 0.02$, and so the percentage change to the bulk-skin temperature difference is correspondingly small (in fact the time average temperature difference is $\mathcal{O}\left(\mathrm{Pe}^2\right)$ in our case, as the linear term time averages to zero.) The small Péclet number expansion (31) may also have important consequences for the parameterisation of the skin temperature in climate models. We can use (31) to asymptotically bound the change in skin temperature induced by any small Péclet number flow satisfying the assumptions of the steady Osborne (1965) theory. This suggests that small Péclet number flows will not generate significant changes in the skin temperature via the skin layer straining mechanism, and as a result will not have a significant impact on the ocean-atmosphere heat transfer. In particular, internal waves cannot generate large changes in sea surface temperature, as compared to the static bulk-skin temperature difference. This may also explain our difficulties in quantifying the effects of small Péclet number flows in the laboratory, as the resulting change in bulk-skin temperature difference is smaller than the resolution of our experimental equipment.

We can also use our results to infer consequences for transfer of dissolved gases between ocean and atmosphere. The non-dimensional representation presented in §2.3 immediately generalises to transport of any other scalar quantity by replacing temperature with gas concentration, thermal diffusivity κ with a gas diffusivity D and defining a corresponding gas flux to replace the heat flux Q. The behaviour of the surface gas concentration is then determined by a Péclet number based on gas diffusivity, $\mathrm{Pe}_D = \alpha\delta^2/D$. If gas diffusion is

significantly slower than thermal diffusion, $D \ll \kappa$, this raises the interesting possibility of having a small thermal Péclet number at the same time as a large gas Péclet number. This is the case for diffusion of dissolved carbon dioxide, with $D/\kappa \approx 0.01$ (Wanninkhof, 1992). Hence, although internal waves have a small effect on sea surface temperature, they may have important consequences for gas transfer. Solutions of the time dependent advection-diffusion equation (19) therefore warrant further consideration so that we can accurately quantify the effects of internal waves on ocean-atmosphere gas transfer.

Acknowledgments I would like to thank all the staff and fellows for providing an excellent working atmosphere and a rewarding summer. In particular, I am grateful to Keith Bradley and Karl Helfrich for their technical assistance and patience in the laboratory. I am also indebted to Claudia Cenedese, Tom Farrar and Chris Zappa for their support, guidance and numerous stimulating discussions throughout the summer.

References

Castro, S. L., Wick, G. A. & Emery, W. J. 2003 Further refinements to models for the bulk-skin sea surface temperature difference. *Journal of Geophysical Research* **108** (C12), doi:10.1029/2002JC001641.

Ewing, G. C. & McAlister, E. D. 1960 On the thermal boundary layer of the ocean. *Science* **131**, 1374–1376.

Fairall, C. W., Bradley, E. F., Rogers, D. P., Edson, J. B. & Young, G. S. 1996 Bulk parameterisation of air-sea fluxes for Tropical Ocean-Global Atmosphere Coupled Ocean-Atmosphere Response Experiment. *Journal of Geophysical Research* **101** (C2), 3747–3764.

Farrar, J. T., Zappa, C. J., Weller, R. A. & Jessup, A. T. 2007 Sea surface temperature signatures of oceanic internal waves in low winds. *Journal of Geophysical Research* **112** (C06014), doi:10.1029/2006JC003947.

Gasparovic, R. F., Apel, J. R. & S., K. E. 1988 An overview of the SAR internal wave signature experiment. *Journal of Geophysical Research* **93** (C10), 12304–12316.

Howard, L. N. 1966 Convection at high Rayleigh number. In *Proceedings of the eleventh international congress of applied mechanics* (ed. H. Görtler), pp. 1109–1115. Springer-Verlag.

Katsaros, K. B. 1980 The aqueous thermal boundary layer. *Boundary-Layer Meteorology* **18**, 107–127.

Katsaros, K. B., Liu, W. T., Businger, J. A. & Tillman, J. E. 1977 Heat transport and thermal structure in the interfacial boundary layer measured in an open tank of water in turbulent free convection. *Journal of Fluid Mechanics* **83**, 311–335.

Leighton, R. I., Smith, G. B. & Handlerb, R. A. 2003 Direct numerical simulations of free convection beneath an air-water interface at low Rayleigh numbers. *Physics of Fluids* **15**, 3181–3193.

Marmorino, G. O., Smith, G. B. & Lindemann, G. J. 2004 Infrared imagery of ocean internal waves. *Geophysical Research Letters* **31** (L11309), doi:10.1029/2004GL020152.

McKenna, S. P. & McGillis, W. R. 2004 The role of free-surface trubulence and surfactants in air-water gas transfer. *International Journal of Heat and Mass Transfer* **47**, 539–553.

Osborne, M. F. M. 1965 The effect of convergent and divergent flow patterns on infrared and optical radiation from the sea. *Deutsche Hydrographische Zeitschrift* **18** (1), 1–25.

Saunders, P. 1967 The temperature at the ocean-air interface. *Journal of Atmospheric Science* **24**, 269–273.

Soloviev, A., Donelan, M., Graber, H., Haus, B. & Schlüssel, P. 2007 An approach to estimation of near-surface turbulence and CO_2 transfer velocity from remote sensing data. *Journal of Marine Systems* **66**, 182–194.

Soloviev, A. V. 2007 Coupled renewal model of ocean viscous sublayer, thermal skin effect and interfacial gas transfer velocity. *Journal of Marine Systems* **66**, 19–27.

Soloviev, A. V. & Schlüssel, P. 1994 Parameterisation of the cool skin of the ocean and of the air-ocean gas transfer on the basis of modeling surface renewal. *Journal of Physical Oceanography* **24**, 1339–1346.

Tennekes, H. & Lumley, J. L. 1972 *A first course in turbulence*, chap. 1, pp. 27–34. MIT.

Walsh, E. J., Pinkel, R., Hagan, D. E., Weller, R. A., Fairall, C. W., Rodgers, D. P., Burns, S. P. & Baumgartner, M. 1998 Coupling of internal waves on the main thermocline to the diurnal surface layer and sea surface temperature during the Tropical Ocean-Global Atmosphere Coupled Ocean-Atmosphere Response Experiment. *Journal of Geophysical Research* **103**, 12613–12628.

Wanninkhof, R. 1992 Relationship between wind speed and gas exchange over the ocean. *Journal of Geophysical Research* **97**, 7373–7382.

Wick, G. A., J., E. W., Kantha, L. H. & Schlüssel, P. 1996 The behaviour of the bulk-skin sea surface temperature difference under varying wind speed and heat flux. *Journal of Physical Oceanography* **26** (10), 1969–1987.

Woodcock, A. H. & Stommel, H. 1947 Temperatures observed near the surface of a fresh-water pond at night. *Journal of Meteorology* **4**, 102–103.

Zappa, C. J. & Jessup, A. T. 2005 High-resolution airborne infrared measurements of ocean skin temperature. *IEEE Geoscience and Remote Sensing Letters* **2** (2), 146–150.